

Anodic and Cathodic Polarization of 1018 Mild Steel and 304 Stainless Steel

MSE 130: Experimental Materials Science and Design

Jonathan Lee

Department of Materials Science and Engineering
University of California, Berkeley

18 October 2020

Contents

1	Abstract	3
2	Introduction	3
2.1	Three Models for Polarization Curve Fitting	3
2.2	Additional Behavior: 1018MS	6
2.3	Additional Behavior: 304SS	7
3	Experimental Procedure	7
4	Results	9
4.1	1018MS Corrosion Parameters from Anodic/Cathodic Sweeps	9
4.2	1018MS Corrosion Parameters from LPR Sweeps	12
4.3	Deconvolution of 304SS H ₂ SO ₄ Polarization Sweep	12
4.4	Deconvolution of 304SS HCl Polarization Sweep	16
5	Discussion	18
5.1	Comments Upon Fitting Procedure Validity	18
5.2	Discussion of Hysteresis in 1018MS Curves	18
5.3	Effect of Chloride Ions on 304SS Passivation Behavior	19
5.4	Anomalous Behavior Following Passivation Potential	20
6	Conclusions	21
7	Acknowledgments	22
8	References	22
9	Appendix 1: Analysis Code and Microscopy Images	23
10	Appendix 2: Additional Butler-Volmer Fits	23
11	Appendix 3: Additional LPR Fits	25

1 Abstract

A series of polarization cell experiments were conducted so as to characterize the corrosion behavior of 1018 mild steel and 304 stainless steel samples when polarized in strongly-acidic solutions, on behalf of an anonymous manufacturer. Three models of varying complexity were employed to fit the data, including a nontraditional modification of the Butler-Volmer equation that incorporated diffusion limitations and the synthesis of passivation barriers. It was found that for the H/Fe redox couple on 1018MS, $j_{\text{corr}} = 1.49\text{e-}6 \text{ A/mm}^2$ and $\Delta\phi_{\text{corr}} = -0.491 \text{ V vs. SCE}$. For 304SS in 1M H_2SO_4 solution, the passivation barrier was found to form at -0.277 V and break down at 0.892 V , while in 1M HCl solution, the barrier formed at -0.157 V and broke down at 0.402 V due to chloride pitting.

2 Introduction

2.1 Three Models for Polarization Curve Fitting

When a metal is placed in solution, there often exists a difference between the metal's work function and the electron energy levels of the solution species. Electrons will therefore transfer between the metal and the solution. Depending on the properties of the resulting metal ions, this may result in the corrosion (dissolution) of the metal body.[1] For example, for the coupled reactions in Equation 1, the Fe^{2+} ions produced are soluble in aqueous solution:



In an isolated system, this redox reaction continues until a the unfavorable charge imbalance cancels the driving force; an equilibrium electrochemical potential difference is thus established. Yet the scenario is modified if this metal electrode is connected to a counter-

electrode of a different metallic species. The counter-electrode may manifest its own redox reactions so as to maintain charge neutrality in the solution; for example, in acidic media, the common Pt counter-electrode may serve as the site of hydrogen oxidation and reduction without itself corroding. Furthermore, any electrochemical potential difference between the electrode and counter-electrode provides a driving force for current flow. The net effect is that a circuit is established that continuously corrodes the electrode.[1]

This scenario is common in engineering situations—for example, the field of marine electronics deals heavily with the fact that the ocean-immersed components of a ship’s hull will corrode if made of dissimilar metals. In the laboratory, it may be replicated within a polarization cell, wherein a sample is immersed in solution with a counter-electrode and a reference electrode against which to measure potential differences (such as the Saturated Calomel Electrode, a Hg-based electrode abbreviated as "SCE"). A potentiostat is used to drive the sample to various potentials relative to SCE; the current required to do so provides a measure of the reactions taking place at the sample surface. Such data sweeps are known as polarization curves.[2]

The corrosion behavior of Fe in acidic solution may be described using the Butler-Volmer equation:

$$j = j_{\text{corr}} \left[\exp \left(\frac{\beta n F}{RT} (\phi - \Delta\phi_{\text{corr}}) \right) - \exp \left(\frac{(1 - \beta) n F}{RT} (\phi - \Delta\phi_{\text{corr}}) \right) \right] \quad (2)$$

In this form of the Bulter-Volmer equation, ϕ is the applied potential relative to SHE. $\Delta\phi_{\text{corr}}$ is the "corrosion potential," at which the rates of Fe oxidation and H reduction at the electrode are equal to each other. The reaction rate at this point is the corrosion rate j_{corr} and manifests as a point where zero current need be supplied by the potentiostat. β encodes any anisotropy between the exchange current densities of the anodic and cathodic reactions and is typically ~ 0.5 ; $n = 2$ is the number of electrons exchanged in the reaction; R is the ideal gas constant; F is the Faraday constant; and T is temperature.[2]

In this analysis, the Butler-Volmer equation will not be used in its full form, but instead in three separate modified forms. The first modification is to condense and rewrite the prefactors:

$$j = j_{\text{corr}} \left[\exp \left(\frac{\ln(10)\eta}{A_{\text{Fe}}} \right) - \exp \left(\frac{\ln(10)\eta}{A_{\text{H}}} \right) \right] \quad (3)$$

In this case, η is shorthand for the overpotential $\phi - \Delta\phi_{\text{corr}}$. A_{Fe} and A_{H} are the Tafel slopes for Fe oxidation and H reduction, respectively, and may be considered as the overpotential required (in volts) to increase the reaction current density by a factor of 10. Fitting 3 to the polarization curve is typically done in the space of $\log_{10} |j|$ vs. η , such that either the anodic or cathodic terms dominate and produce linear behavior far from $\Delta\phi_{\text{corr}}$, while a singularity exists at $\Delta\phi_{\text{corr}}$ itself.[2]

The second modification is to consider the Butler-Volmer equation in the small- η regime, i.e. at potentials close to $\Delta\phi_{\text{corr}}$ vs. SHE. A Taylor expansion of Equation 2 reveals linear behavior:

$$j = j_{\text{corr}} \frac{nF}{RT} \eta \quad (4)$$

For the Fe/H corrosion couple, the nF/RT prefactor has a value of 77.85 V^{-1} at 25°C . The corrosion potential may therefore be determined by a linear fit to a "Linear Polarization Resistance" (LPR) scan at small overpotentials (colloqually defined as $|\eta| < 100 \text{ mV}$).[2]

The third modification is to account for the limitations of ion diffusion: at large overpotentials, a diffusion barrier may slow the rate of reaction, producing a smaller current than would be expected from Equation 2. Such diffusion barriers comprise complicated effects such as charge double-layers and may manifest themselves nonlinearly due to reaction kinetics, but as a rudimentary approximation, the barrier is assumed to have a constant resistivity ρ_{bar} . As such, a given half-reaction in Equation 2 will tend towards ohmic behavior at high currents, while Equation 2 itself describes electrical behavior comparable to a diode.[2] The

model in Reference [3] for a diode and resistor in series may be used as a guide to derive:

$$j = \frac{1}{B_0 \rho_{\text{bar}}} W(B_0 j_0 \rho_{\text{bar}} \exp(B_0 \eta)) \quad (5)$$

In this equation, B_0 is defined as $\ln(10)/A_0$ where A_0 is the Tafel-slope of the half-reaction, while W_0 is the 0-th branch of the Lambert W function. Since this equation is presented for a half-reaction, the parameters are defined in terms of a reference potential $\Delta\phi_{\text{ref}}$ and reference current j_0 instead of a corrosion potential and current, which only have meaning for a reaction couple.

2.2 Additional Behavior: 1018MS

1018MS (0.15-0.20 wt% C, 0.60-0.90 wt% Mn, bal. Fe) possesses a heterogenous microstructure consisting of a nearly-carbonless ferrite α -phase and the high-carbon Fe_3C cementite phase.[4] The fabrication of this steel involves quenching through a two-phase $\alpha + \gamma$ region; as a result, the original volumes of γ -phase become "pearlite," comprising dense lamellae of ferrite and cementite. An inspection of the Fe phase diagram for 0.18 wt% C indicates that 1018MS globally contains 2.7 wt% cementite, concentrated within pearlite regions that comprise 20 wt% of the microstructure. Cementite therefore comprises 14 wt% of the pearlite regions. For this analysis, the alloying element Mn is ignored.

This microstructure is generally expected to have a pronounced effect on the corrosion behavior of 1018MS. Cementite does not corrode as the high-Fe α -phase does, yet it conducts metallicity and catalyzes the H^+ reduction reaction. Specifically, the exchange current density on Fe_3C for hydrogen reduction is several orders of magnitude higher than on the α -phase. As the α -phase corrodes away, Fe_3C lamellae are left behind, producing a large increase in the area available for Fe_3C to catalyze the reaction. This means that as the 1018MS electrode corrodes, the parameters of Equation 3 should shift towards greater corrosion currents in the cathodic regime.[4]

2.3 Additional Behavior: 304SS

304SS (18 wt% Cr, 8 wt% Ni, bal. Fe) is designed to self-passivate in acidic solution above certain overpotentials. Specifically, at a passivation potential $\Delta\phi_{\text{pass}} > \Delta\phi_{\text{corr}}$, Cr atoms oxidize into a +3 state in the form of a "passivation layer" consisting primarily of Cr_2O_3 . Despite being only a few unit cells thick, this passivation layer provides an extremely-effective barrier against continued Fe oxidation; above the $\Delta\phi_{\text{pass}}$, the electrode current in a passivation sweep is nearly flat.[1]

This passivated regime, however, has an upper limit resulting from a "breakdown potential" ($\Delta\phi_{\text{breakdown}}$) at which Cr_2O_3 begins to oxidize into aqueous HCrO_4^- ions (+6 Cr oxidation state).[4] In the presence of chloride ions, the limit is instead dictated by "pitting potential" ($\Delta\phi_{\text{pit}}$), wherein Cl^- ions locally attack the passivation barrier in a self-catalyzed reaction, thus locally restoring Fe corrosion behavior. This pitting potential typically occurs before the passivation layer breakdown potential; as such, the passivation regime in HCl is expected to be smaller than in H_2SO_4 . [2]

3 Experimental Procedure

1/8" diameter rods of 304SS and 1018MS were cut into cylindrical samples, then sanded with 600-grit paper and rinsed with deionized water so as to clean their surfaces.[4] In total, four samples were produced (2x 304SS and 2x 1018MS). The samples were imaged under an optical microscope so as to provide a reference against which to compare their corroded surfaces.

Each sample was installed as the working electrode within a polarization cell, alongside a platinum counter-electrode and a saturated calomel reference electrode (SCE). So as to minimize the effects of solution resistivity on the measured voltage, the reference electrode was contained within a Luggers-Habin probe, of which the capillary tip was placed at the midpoint of the sample. The polarization cell was filled with either 250 mL of 1M HCl

solution or 250 mL of 1M H₂SO₄ solution. The Luggin-Haber probe was filled with the same chosen solution to a surface level 1/4" below that of the polarization cell; this precluded the contamination of the polarization cell with 4M Cl⁻ solution from the SCE reference. Care was taken during filling to avoid bubbles, as well as to position the Luggin-Haber probe in a way that would not allow bubbles to enter its capillary during the course of the experiment.[4] Sample dimensions, solutions, and immersion lengths are recorded in Table 1.

Sample	Materials	Soln	Diameter	Immersed Length
1	1018MS	H ₂ SO ₄	3.12 mm	14.8 mm
2	1018MS	HCl	3.12 mm	15.6 mm
3	304SS	H ₂ SO ₄	3.12 mm	16.1 mm
4	304SS	HCl	3.12 mm	13.6 mm

Table 1: Sample dimensions used to calculate critical current densities from the collected current data.

Scan	Sample	Solution	Classification	Sweep Rate (mV/sec)
0	1018MS	H ₂ SO ₄	Ano/Cat	10 mV/sec
1	1018MS	H ₂ SO ₄	LPR	1 mV/sec
2	1018MS	H ₂ SO ₄	Ano/Cat	10 mV/sec
3	1018MS	H ₂ SO ₄	LPR	1 mV/sec
4	1018MS	HCl	Ano/Cat	10 mV/sec
5	1018MS	HCl	LPR	1 mV/sec
6	1018MS	HCl	Ano/Cat	10 mV/sec
7	1018MS	HCl	LPR	1 mV/sec
8	304SS	H ₂ SO ₄	Cathodic	10 mV/sec
9	304SS	H ₂ SO ₄	Anodic	10 mV/sec
10	304SS	HCl	Cathodic	10 mV/sec
11	304SS	HCl	Anodic	10 mV/sec

Table 2: General description of the 12 collected polarization curves.

The three electrodes were connected to a potentiostat constructed by previous laboratory personnel (10V compliance voltage, 190 mA maximum current, 200 mA thermal fuse cutoff, 15pA reference input current, 1e-6 mA current sensitivity, 2% current accuracy).[2, 4] The approximate location of the H/Fe corrosion potential was identified, after which various polarization sweeps were conducted for each sample. Twelve polarization sweeps were collected

in total; the overall classification of each sweep are enumerated in Table 2. The parameters of each type of sweep were:

- 1018MS Anodic/Cathodic Sweep (“AnoCat”): upward scan from 200 mV below $\Delta\phi_{\text{corr}}$ to the potential above $\Delta\phi_{\text{corr}}$ that produced 1 mA anodic current, followed by a reverse scan to return to the starting potential.
- 1018MS Linear Polarization Resistance Sweep (“LPR”): immediately after an Ano/Cat sweep, potential held 200 mV below $\Delta\phi_{\text{corr}}$ until the current stabilized; after which an upward scan from 20 mV below $\delta\phi_{\text{corr}}$ to 20 mV above $\delta\phi_{\text{corr}}$ and back was performed.
- 304SS Cathodic Sweep: downward scan from 20 mV above $\Delta\phi_{\text{corr}}$ to 700 mV below $\Delta\phi_{\text{corr}}$.
- 304SS Anodic Sweep: upward scan from 20 mV below $\Delta\phi_{\text{corr}}$ to the potential that achieved the maximum potentiostat current of 190 mA, followed by a downward scan until a transition to cathodic behavior was observed.[4]

It should be noted that the 304SS Anodic sweep in HCl required reversing the scan direction in the vicinity of 100 mA instead of near the maximum potentiostat current, since Cl^- pitting was predicted to produce a rise in current even after the potential was decreased.[4]

After the sweeps were concluded, the samples were dried and imaged once more under an optical microscope at magnifications of 5x, 10x, and 20x. Microscopy images are contained within Appendix 1.

4 Results

4.1 1018MS Corrosion Parameters from Anodic/Cathodic Sweeps

All collected 1018MS polarization sweeps were fit to the form of Equation 3 using the Python package *lmfit*. [5] Since Equation 1 does not account for diffusion-limited behavior, each fitting

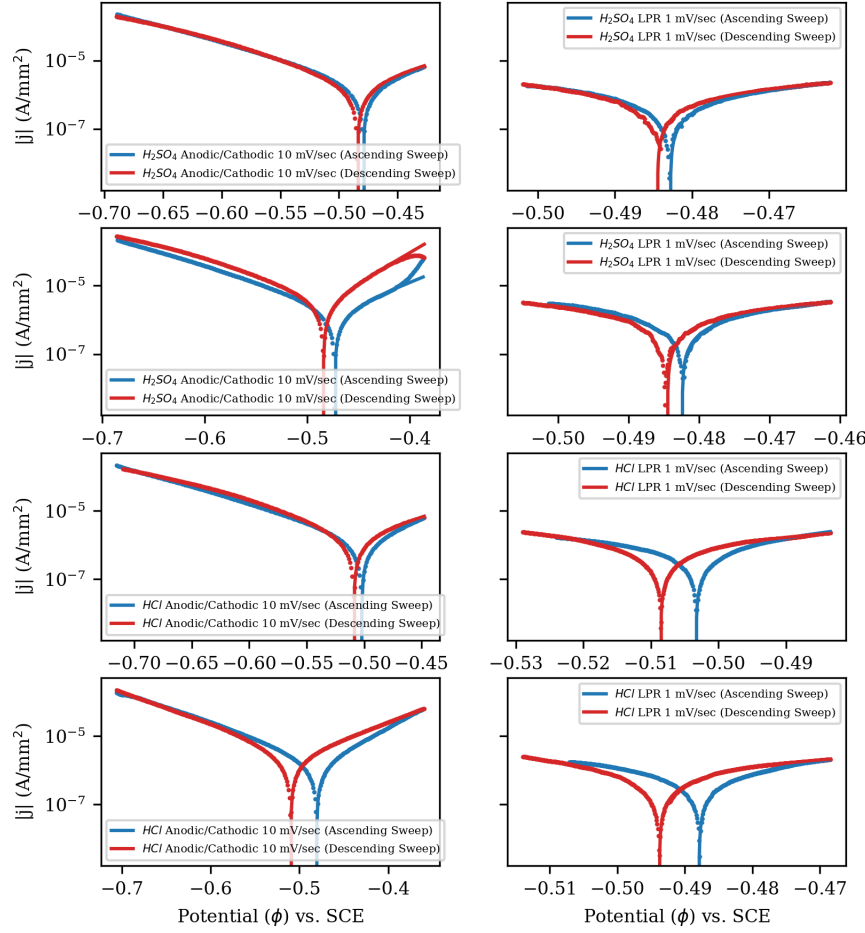


Figure 1: Results of fitting Equation 3 to the eight 1018MS polarization sweeps. The scales of the axes indicate little variation in the current densities and potentials relative to SCE among the sweeps, though the limited scope of the LPR sweeps produced a large variance in their calculated parameters.

was performed within a narrow data window of width 100 mV centered on the corrosion potential. The quality of fits varied: while the parameters derived from the LPR scans possessed much smaller variances due to their greater data densities, the parameters derived from the Ano/Cat scans were far more consistent in terms of value. The fitted parameters and variances from the designated Ano/Cat scans are presented in Table 3, while the according fits are plotted against the data in Figure 1. All fitted parameters for the eight 1018MS

Scan	Soln	Dir	A_H (V)	A_{Fe} (V)	j_{corr} (A/mm ²)	$\Delta\phi_{corr}$ (V)
0	H ₂ SO ₄	Asc	-8.778e-02	8.903e-02	1.784e-06	-4.794e-01
		Des	-9.588e-02	8.833e-02	1.888e-06	-4.843e-01
2	H ₂ SO ₄	Asc	-8.341e-02	8.519e-02	1.663e-06	-4.730e-01
		Des	-5.730e-02	8.076e-02	3.096e-06	-4.842e-01
4	HCl	Asc	-7.706e-02	8.553e-02	1.277e-06	-5.022e-01
		Des	-9.978e-02	8.326e-02	1.765e-06	-5.090e-01
6	HCl	Asc	-7.490e-02	9.225e-02	1.469e-06	-4.806e-01
		Des	-1.035e-01	8.415e-02	2.140e-06	-5.097e-01

Table 3: Derived parameters for Equation 3 (Tafel slopes, corrosion currents, and corrosion potentials relative to SCE) for 1018MS anodic/cathodic sweeps. See Appendix 2 for associated variances.

scans, as well as their variances, may be found in Appendix 2.

Using solely the data from the Ano/Cat scans (Scans 0, 2, 4, and 6), the average values of the Tafel slopes were found to be $A_H = -8.620\text{e-}02$ V and $A_{Fe} = 8.606\text{e-}02$ V; the similarity in the magnitude of these values supports the assumption that $\beta \approx 0.5$ in Equation 2. The average corrosion potential was found to be $\Delta\phi_{corr} = -0.4903$ V vs. SCE, with the associated average corrosion rate being $j_{corr} = 1.88\text{e-}6$ A/mm². The variances in the equilibrium parameters were much smaller than their respective values ($\sigma^2(j_{corr}) = 2.14\text{e-}15$ A/mm², $\sigma^2(\Delta\phi_{corr}) = 5.41\text{e-}8$ V), but the variances of the Tafel slopes were found to be uncharacteristically large ($\sigma^2(A_H) = 99.5$ V, $\sigma^2(A_{Fe}) = 159$ V). Given the similarities of the actual fitted parameters, however, this was thought to be an error in statistical estimation rather than an indicator of actual variance in the Tafel slopes.

It should be noted that, in this analysis, variances were propagated using:

$$f(a_1, a_2, \dots) \rightarrow \sigma_f^2 = \sum_i \left(\frac{\partial f}{\partial a_i} \right)^2 \sigma_{a_i}^2 \quad (6)$$

It should also be noted that hysteresis was observed within these scans; the observed corrosion potentials on the downward half of the sweeps were consistently lower than those of the upward halves. A discussion of this hysteresis is reserved for the Discussion.

4.2 1018MS Corrosion Parameters from LPR Sweeps

Scan	Soln	Dir	j_{corr} (A/mm ²)	$\Delta\phi_{\text{corr}}$ (V)	$\sigma^2(j_{\text{corr}})$	n
1	H ₂ SO ₄	Asc	1.342e-06	-4.830e-01	6.559e-16	338
		Des	1.354e-06	-4.841e-01	3.434e-15	421
3	H ₂ SO ₄	Asc	2.058e-06	-4.822e-01	2.552e-15	342
		Des	1.941e-06	-4.849e-01	1.070e-14	444
5	HCl	Asc	1.302e-06	-5.032e-01	4.275e-14	353
		Des	1.335e-06	-5.085e-01	2.300e-14	442
7	HCl	Asc	1.265e-06	-4.879e-01	4.494e-15	342
		Des	1.297e-06	-4.937e-01	2.720e-14	443

Table 4: Fitting parameters for Equation 4, as calculated from the LPR scans for 1018MS. The fitting package *lmfit* was unable to estimate the variance for $\Delta\phi_{\text{corr}}$.

Figure 2 shows the results of fitting Equation 4 to local linear regions of each of the 1018MS scans. In the case of the dedicated LPR scans, this region comprised the entirety of the scans, while the Ano/Cat scans were trimmed to a window of $\Delta\phi_{\text{corr}} \pm 20$ mV in order to isolate a comparable region. All 1018MS scans were found to possess linear behavior in the vicinity of $\Delta\phi_{\text{corr}}$, validating the LPR measurement approach. The resulting parameters from the pre-designated LPR scans (Scans 1, 3, 5, and 7) are shown in Table 4, while the fitted parameters for all eight 1018MS scans are presented in Appendix 3.

Using these data, the average value for the corrosion current was found to be 1.49e-6 A/mm², with an associated variance of $\sigma^2(j_{\text{corr}}) = 1.79\text{e-}15$ A/mm². The average value of the corrosion potential was found to be -4.910 V, though *lmfit* estimated the variances of this parameter to be 0.

4.3 Deconvolution of 304SS H₂SO₄ Polarization Sweep

In order to analyze the 304SS polarization curves, the anodic and cathodic sweeps were concatenated. In the case of the HCl curves, this did not require any modification; however, the cathodic H₂SO₄ curve exhibited a corrosion potential ~ 0.25 V higher than any other corrosion potential measured in this experiment. This was assumed to be an experimental

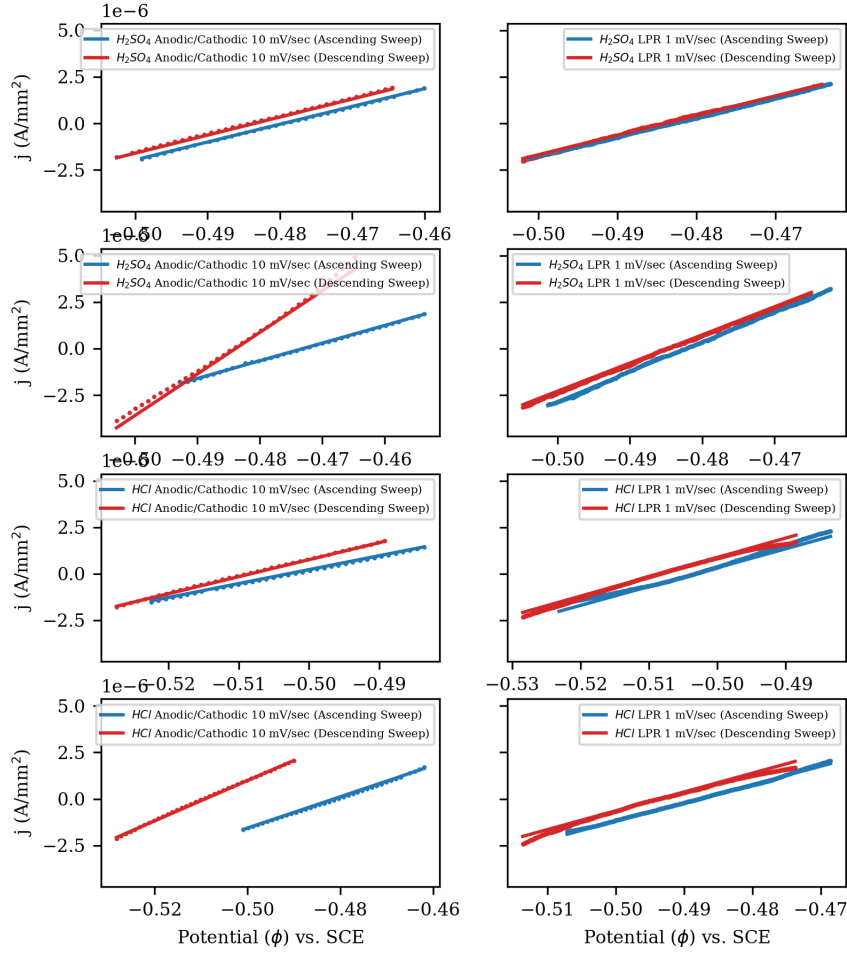


Figure 2: Linear fits in the low-overpotential regime for all eight 1018MS scans.

error; so such, the data were shifted so that their corrosion potential aligned with that of the anodic curve.

For both the H_2SO_4 and HCl curves, the hydrogen reduction reaction was fit to the diffusion-limited model (Equation 5) and subtracted out of the remaining data. This was observed, however, to have little effect. In particular, this deconvolution did not remove any other singularities or depressions in the curves, indicating that other reduction reactions were active within certain ϕ -regimes. The dominant reactions in portions of the H_2SO_4 curve were thus explained as follows:

- **< ~-0.4 V:** $2\text{H}^+ + 2e^- \rightarrow \text{H}_2$ (reduction of hydrogen ions to produce hydrogen gas, as evidenced by bubbling on the electrode surface)
- **~-0.4 V to ~-0.3 V:** $\text{Fe} \rightarrow \text{Fe}^{2+} + 2e^-$ (oxidation and dissolution of iron)
- **~-0.3 V to ~0 V:** $\text{Cr} \rightarrow \text{Cr}^{3+} + 3e^-$ (passivation of electrode surface due to formation of Cr_2O_3 , and intersection with an unknown reduction reaction, such as the reduction of aqueous Fe, Ni, or Cr)
- **~0 V to ~0.9 V:** $\text{Cr} \rightarrow \text{Cr}^{3+} + 3e^-$ (passivation of electrode surface due to formation of Cr_2O_3)
- **~0.9 V to ~1.5 V:** $\text{Cr}^{3+} \rightarrow \text{Cr}^{6+} + 3e^-$ (destruction of passivation layer to formation of aqueous HCrO_4^- , as evidenced by reddish-orange ion trails surrounding the electrode)
- **> ~1.5 V:** $\text{H}_2\text{O} \rightarrow 2\text{H}^+ + \frac{1}{2}\text{O}_2 + 2e^-$ (breakdown of water, as evidenced by renewed bubbling on the electrode surface)
- **< ~0.8 V on descending sweep:** $\text{Cr}^{6+} + 3e^- \rightarrow \text{Cr}^{3+}$ (reduction of aqueous Cr to reconstruct the passivation layer)

An attempt was then made to deconvolute the H_2SO_4 curve into contributions from its component reactions, as modelled using Equation 5. It was found, however, that Equation 5 could not fit the passivation region; furthermore, the presence of multiple singularities precluded a traditional stepwise model of the passivation potential, which would not be able to manifest the changes in concavity required to replicate these singularities. Equation 5 was therefore modified by means of a changing resistivity:

$$\rho = \rho_{\text{lim}} + \rho_{\text{pass}} [1 - \exp(-\alpha_{\text{pass}} \eta_{\text{pass}}^3)] \quad (7)$$

This “ansatz” treats the passivation layer as an additional resistivity in series with that of the diffusion layer. Its two-dimensional formation is modeled using Johnson-Mehl-Avrami-Kolmogorov kinetics.[6] Since the potential ramp rate is constant throughout the curve, time in the JMAK equation was replaced with the overpotential relative to the passivation potential (η_{pass}). Such a form produces an s-curve that, while having no rigorous theoretical basis, nevertheless provides an improved fitting approximation of regions of the polarization

Reaction	ϕ_0 (V)	j_0 (A/mm ²)	A (V)	ρ_{lim} ($\Omega \cdot \text{mm}$)
H ⁺ reduction	-3.728e-01	-9.612e-08	-1.138e-01	1.587e+02
Fe oxidation (passivation-limited)	-3.927e-01	7.891e-07	3.505e-03	3.905e+04
Cr ₂ O ₃ barrier breakdown (asc)	9.688e-01	9.902e-07	3.701e-02	1.968e+03
H ₂ O breakdown (asc)	1.596e+00	1.065e-04	2.025e-01	3.230e-312
unknown reduction reaction	1.500e-01	-5.000e-11	-3.289e-02	2.000e+05
Cr ₂ O ₃ solution deposition	1.070e+00	-1.812e+169	-9.784e-06	4.502e+06
Cr ₂ O ₃ barrier breakdown (desc)	9.814e-01	4.565e-07	5.713e-02	1.324e+03
H ₂ O breakdown (desc)	1.599e+00	1.016e-04	1.971e-01	3.765e-06

Reaction	ϕ_{pass} (V)	α_{pass} (V ⁻³)	ρ_{pass} ($\Omega \cdot \text{mm}$)
Fe oxidation (passivation-limited)	-3.530e-01	4.814e+00	6.966e+06
Cr ₂ O ₃ barrier breakdown (asc)	1.300e+00	8.971e-03	5.670e+07
unknown reduction reaction	-3.000e-02	1.000e+01	1.000e+07
Cr ₂ O ₃ barrier breakdown (desc)	1.239e+00	7.470e-03	2.868e+07

Table 5: Deconvolution parameters for Equation 5 from the combined anodic/cathodic H₂SO₄ polarization sweep. Four fitting regions required the JMAK resisitivity modification outlined in Equation 7.

curve. The results of the deconvolution of the H₂SO₄ into individual reaction components are presented in Table 5, while the resulting curves are presented in Figure 3.

From this analysis, the passivation potential $\Delta\phi_{\text{pass}}$ might be defined as the “nucleation” potential for the passivation barrier described in Equation 7. For the case of H₂SO₄, this was fitted as -0.353 V. Meanwhile, a more conventional approach might be to consider the passivation potential as the potential corresponding to the maximum observed dissolution rate; in this case, this is -0.277 V, corresponding to a dissolution rate of 2.15e-6 A/mm². It should further be noted that the end of the passivation regime may be quantified by the crossover corresponding to the Cr III/Cr VI redox couple on the reverse-sweep, fitted to be 0.892 V vs. SCE. This value is 9.99% below the the literature value (0.991 V vs. SCE).

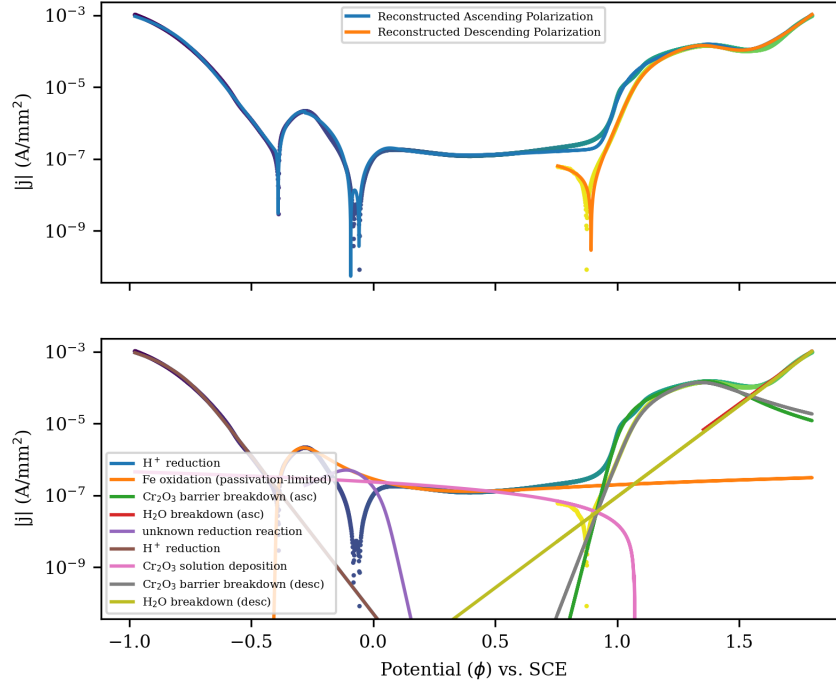


Figure 3: Top: Fitted H_2SO_4 curves generated by deconvolution procedure. Bottom: Individual reaction components fitted using Equations 5 and 7.

4.4 Deconvolution of 304SS HCl Polarization Sweep

Following the same procedure as with the H_2SO_4 sweep, the dominant reactions over the course of the HCl curve were proposed to be:

- **$< \sim -0.4 \text{ V}$:** $2\text{H}^+ + 2e^- \rightarrow \text{H}_2$ (reduction of hydrogen ions to produce hydrogen gas, as evidenced by bubbling on the electrode surface)
- **$\sim -0.4 \text{ V}$ to $\sim 0.2 \text{ V}$:** $\text{Fe} \rightarrow \text{Fe}^{2+} + 2e^-$ (oxidation and dissolution of iron)
- **$\sim 0.2 \text{ V}$ to $\sim 0.3 \text{ V}$:** $\text{Cr} \rightarrow \text{Cr}^{3+} + 3e^-$ (passivation of electrode surface due to formation of Cr_2O_3)
- **$> \sim 0.3 \text{ V}$:** destruction of passivation layer though Cl^- pitting
- **$< \sim 0.5 \text{ V}$ on descending:** autocatalytic Cl^- pitting (eventual restoration of passivation barrier)

The resulting fitting parameters are summarized in Table 6, while the deconvolved curves

are presented in Figure 4. The fitted corrosion potential was found to be -0.164 V, while the maximum Fe corrosion rate of $8.43\text{e-}4 \text{ A/mm}^2$ appeared at -0.157 V vs. SHE. No post-passivation singularities were observed.

Reaction	ϕ_0 (V)	j_0 (A/mm ²)	A (V)	ρ_{lim} ($\Omega\cdot\text{mm}$)
H ⁺ reduction	-3.478e-01	-3.793e-07	-1.145e-01	3.210e+02
Fe oxidation (diffusion-limited)	-4.695e-01	1.498e-08	3.570e-02	2.157e+03
Fe oxidation (passivation-limited)	-4.695e-01	1.498e-08	3.570e-02	2.157e+03
Cl ⁻ ion pitting	3.928e-01	8.802e-05	4.837e-02	9.837e+01

Reaction	ϕ_{pass} (V)	α_{pass} (V ⁻³)	ρ_{pass} ($\Omega\cdot\text{mm}$)
Fe oxidation (passivation-limited)	-1.643e-01	5.187e+03	5.946e+03

Table 6: Deconvolution parameters for Equations 5 and 7 from the combined anodic/cathodic H₂SO₄ polarization sweep.

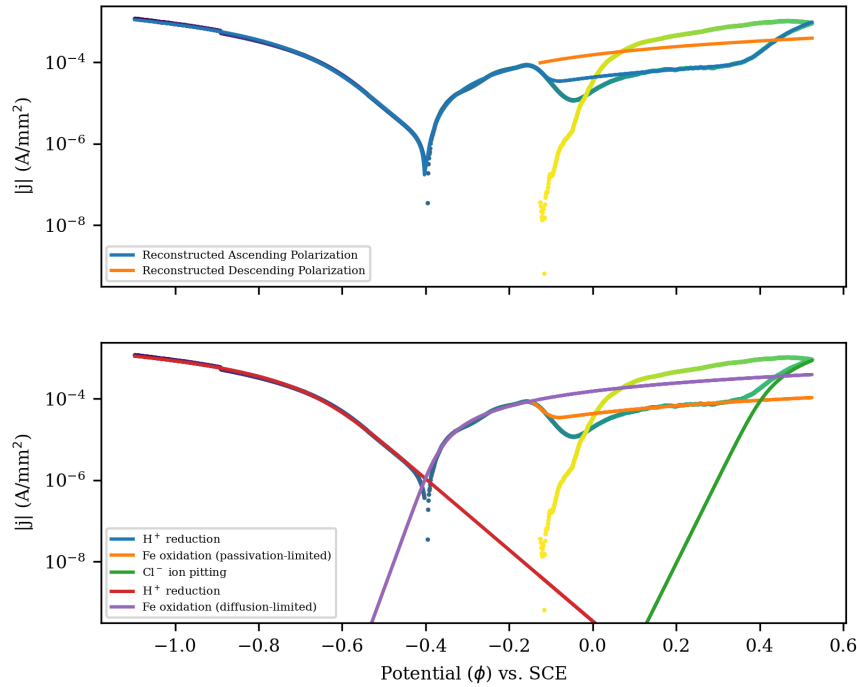


Figure 4: Top: Fitted HCl curves generated by deconvolution procedure. Bottom: Individual reaction components fitted using Equations 5 and 7.

5 Discussion

5.1 Comments Upon Fitting Procedure Validity

In the above analyses, three different fitting procedures were deployed: (1) a Butler-Volmer equation using Tafel slopes, as described by Equation 3; (2) a linearized Butler-Volmer equation applied in the low- η limit following Equation 4; and (3) a generalized diffusion and passivation half-reaction model described by Equations 5 and 7. Of the three, only the linearized model appears to produce consistent and reliable results, as qualified by the low variances of its fitted parameters.

The Tafel-slope equation produced consistent results across multiple scans, but a possible fitting artifact produced variances that were several orders of magnitude larger than the parameters themselves. This might be attributed to the fact that variances lose meaning when applied to non-linear and non-gaussian models; a better way of parameterizing uncertainty in such situations might be to introduce Monte Carlo noise into the dataset.[7]

Meanwhile, the decision was made not to estimate variances for the 304SS deconvoluted curves. The author wishes to emphasize that this procedure was highly subjective in nature; the results depended heavily on the initial seed parameters provided to *lmfit*. The deconvolution was nevertheless an instructive exercise; the model may have utility in the future design of a rigorous fitting algorithm.

5.2 Discussion of Hysteresis in 1018MS Curves

As seen in Figure 1, the 1018MS Ano/Cat and LPR curves all exhibited hysteresis between the upward and downward portions of the sweep; the downward portion consistently manifested a more-negative corrosion potential.

Recalling the discussion in the Introduction regarding the microstructure of 1018MS, one might attempt to explain this hysteresis via hydrogen reduction catalysis by the exposed Fe_3C lamellar microstructure. The hysteresis, however, runs in direct contradiction to the

predicted effects of such a catalysis, which would enhance the exchange current density of the reduction reaction and elevate the current at potentials more negative than $\Delta\phi_{\text{corr}}$. As a result, $\Delta\phi_{\text{corr}}$ would shift to more positive values, since the catalyzed H^+ reduction reaction would be able to match the rate of Fe oxidation at a lower driving force. Yet the hysteresis manifests as a shift in the opposite direction, implying that it is the exchange current of Fe oxidation that has instead been elevated.

One possible mechanism to explain this behavior would be the formation of a passivating oxide on the sample surface in between polarization sweeps. Such a layer would depress the exchange current density of the Fe reduction reaction on the upward sweep, but once it had been ablated by vigorous Fe corrosion at positive overpotentials, it would no longer effect the exchange current density. As such, the exchange current density on the down-sweep would appear elevated. It is also possible that the alloying Mn in the 1018MS plays a role, though this has not been investigated.

In summary, the hysteretic behavior of the 1018MS polarization curves appears anomalous. Further investigation is warranted to determine its causes. The magnitude of the hysteresis, however, is consistently less than ~ 0.5 V; it is up to the manufacturer's discretion to determine if this is acceptable.

5.3 Effect of Chloride Ions on 304SS Passivation Behavior

A post-experiment inspection of the surface structure of the 304SS HCl sample demonstrated that Cl^- pitting had occurred, and therefore that the proposed reaction model and deconvolution were appropriate. (See microscopy images in Appendix 1.)

The maximum dissolution rate in HCl solution was found to be $8.43\text{e-}4$ A/ mm^2 at a potential of -0.157 V; these rate is 392 times larger than the maximum dissolution rate observed in H_2SO_4 solution ($2.15\text{e-}6$ A/ mm^2 at -0.277 V). It therefore appeared that the presence of chloride ions produces a marked increase in the maximum active dissolution rate, as well as shifts this maximum rate to a higher potential. This horizontal shift may

be understood as a change in the passivation behavior of 304SS in the presence of chloride ions. This is not particularly surprising; Reference [8] notes that such ions are actually incorporated into the passivation layer, thereby changing its chemistry.

The similarity among the 1018MS curves for the two solutions, as well as the fact that the entire HCl polarization curve (even within the H^+ reduction regime) was found to be ~ 2 orders of magnitude higher in terms of current density compared to the H_2SO_4 curve, suggests that this may be attributed to some manner of systematic error, effects of Cl^- notwithstanding. This set of experiments was designed simply to map the polarization curve and not to effectively quantify the difference in maximum corrosion rate; additional characterization is necessary to properly make this comparison.

The mapping and deconvolution of the 304SS HCl curve was, however, instructive in terms of other metrics. For example, by defining the Cl^- pitting potential as the point when the current contributions of the fitted Cl^- component exceeded the passivation current, $\Delta\phi_{\text{pitt}}$ was found to be 0.402 V vs. SCE. (It should be noted that this pitting current is actually a “pseudo-current” that has its basis in localized Fe oxidation reactions.

5.4 Anomalous Behavior Following Passivation Potential

There remain two anomalies within the 304SS H_2SO_4 polarization curves that must be discussed: the 9.99% shift of the Cr III/Cr VI corrosion potential below its literature value; and the phenomenon of current depression/inversion in the region immediately following the passivation potential.

The first phenomenon may be readily explained by qualitative inspection of the deconvoluted components of the polarization curve. As shown in Figure 3, the fitted component corresponding to the breakdown of water runs close to the singularity corresponding to the Cr III/Cr VI corrosion potential, providing an additional oxidative component. This would have the effect of pushing the equilibrium potential more negative, since a greater rate of Cr VI reduction would be required to counterbalance the current produced by the break-

down of water. Furthermore, Cr oxidation in this regime is a rate-limiting process for Fe oxidation—any Cr dissolution produces a comparable dissolution of Fe, further enhancing the manifested anodic current.

The second phenomenon, however, is not so straightforwardly explained. The deconvolution procedure demonstrated that it is possible to replicate this feature using components of the form of Equation 5 with the JMAK-type resistivity modification of Equation 7. In particular, the double-singularity phenomenon at a potential of ~ -0.1 V in the H_2SO_4 curve may be replicated using a reduction reaction that is heavily “passivated” at more negative potentials. Oxygen reduction was categorically disqualified as a candidate; in such solutions as 1M HCl and 1M H_2SO_4 , oxygen gas has a low solubility,[4] while an inspection of the electrode surface near the solution/air interface did not yield evidence of any increased corrosion. Chemical species from the counter-electrode were also disqualified; the Pt counter-electrode was specifically chosen such that it would not corrode into the solutions.[1]

Instead, the behavior of the curve suggests that this effect comes from the reduction of an aqueous species that was generated by the corrosion of the sample itself (i.e. the reduction of ions of Fe, Ni, Cr, or other alloying elements). The procedure did not provide a rigorous means of identifying the involved species; in particular, the fitting behavior in this region is heavily dependent upon the curvature of the fitted Fe passivation component. Once again, a more rigorous analysis would be required in order to properly characterize this region, but the deconvolution yields an important conclusion: this is a transient effect based upon a modified solution chemistry, and as such, the manufacturer should not construe it as improved passive properties in its 304SS samples.

6 Conclusions

These polarization cell experiments examined the corrosion behavior of samples of 1018MS and 304SS submitted by an anonymous manufacturer for quality control purposes. Three models were employed to fit the data: a classic Butler-Volmer model; a low-overpotential

linear limit of the Butler-Volmer equation; and a heavily-modified single-component model that employed the Lambert W function and JMAK kinetics in order to model diffusion limitations and passivation effects. The first model yielded $j_{\text{corr}} = 1.88\text{e-}6 \text{ A/mm}^2$, $\Delta\phi_{\text{corr}} = -0.4903 \text{ V}$, $A_{\text{H}} = -8.620\text{e-}2 \text{ V}$, and $A_{\text{Fe}} = 8.606\text{e-}2 \text{ V}$, though these values were marred by large variances. The LPR-derived values of $j_{\text{corr}} = 1.49\text{e-}6 \text{ A/mm}^2$, $\Delta\phi_{\text{corr}} = -0.491 \text{ V}$ were found to be more reliable. An inspection of the 304SS polarization curves yielded a maximum active corrosion rate of $2.15\text{e-}6 \text{ A/mm}^2$ at $\Delta\phi_{\text{pass}} = -0.277 \text{ V}$ for H_2SO_4 and $8.43\text{e-}4 \text{ A/mm}^2$ at $\Delta\phi_{\text{pass}} = -0.157 \text{ V}$ for HCl , while the passivation barrier broke down at the Cr III/Cr VI corrosion potential (0.892 V) in H_2SO_4 and the Cl^- pitting potential (0.402 V) in HCl . This analysis should provide the manufacturer a basic understanding of their steel alloys in terms of these parameters, as well as provide areas of inquiry for the manufacturer to improve their understanding with future investigations.

7 Acknowledgments

The author wishes to thank Chris Kumai of the UC Berkeley MSE department for data collection, as well as GSI Tingzheng Hou for helpful suggestions.

8 References

- ¹T. M. Devine, *Mse 130 lab 2 lectures*, 2020.
- ²T. Hou, *MSE 130 Laboratory: Anodic and Cathodic Polarization of 1018 Mild Steel and 304 Stainless Steel (Discussion Slides)*, tech. rep. (Department of Materials Science and Engineering, University of California, Berkeley, 2020).
- ³T. Banwell and A. Jayakumar, “Exact analytical solution for current flow through diode with series resistance”, *Electronics Letters* **36**, 291–292 (2000).

⁴T. M. Devine, *MSE 130 Laboratory: Anodic and Cathodic Polarization of 1018 Mild Steel and 304 Stainless Steel*, tech. rep. (Department of Materials Science and Engineering, University of California, Berkeley, 2020).

⁵*Lmfit: non-linear least-squares minimization and curve-fitting for python*, <https://lmfit.github.io/lmfit-py/>, 2020.

⁶D. C. Chrzan, *MSE 130 Laboratory: Nucleation and Growth During the Crystallization of Amorphous Te Thin Films*, tech. rep. (Department of Materials Science and Engineering, University of California, Berkeley, 2020).

⁷J. S. Alper and R. I. Gelb, “Standard errors and confidence intervals in nonlinear regression: comparison of monte carlo and parametric statistics”, *J. Phys. Chem.* **94**, 4747–4751 (1990).

⁸L. Wegrelius et al., “Passivation of stainless steels in hydrochloric acid”, *Journal of the Electrochemical Society* **146**, 1397–1406 (1999).

9 Appendix 1: Analysis Code and Microscopy Images

Given the amount of code used to perform the calculations in this report, it is unfeasible to include the source files in an Appendix. Instead, the code may be accessed at https://github.com/jjlee1998/MSE130L_Lab2. The repository also contains the microscopy images referred to throughout this report, which could not be attached here due to size and technical issues.

10 Appendix 2: Additional Butler-Volmer Fits

Scan	Type	Soln	Dir	A_{H} (V)	A_{Fe} (V)	j_{corr} (A/mm ²)	$\Delta\phi_{\text{corr}}$ (V)
0	Ano/Cat	H ₂ SO ₄	Asc	-8.778e-02	8.903e-02	1.784e-06	-4.794e-01
			Des	-9.588e-02	8.833e-02	1.888e-06	-4.843e-01
1	LPR	H ₂ SO ₄	Asc	-8.695e-02	9.256e-02	1.971e-06	-4.828e-01
			Des	-2.030e-01	1.043e-01	3.215e-06	-4.845e-01
2	Ano/Cat	H ₂ SO ₄	Asc	-8.341e-02	8.519e-02	1.663e-06	-4.730e-01
			Des	-5.730e-02	8.076e-02	3.096e-06	-4.842e-01
3	LPR	H ₂ SO ₄	Asc	-6.012e-02	5.633e-02	1.907e-06	-4.824e-01
			Des	-1.807e+03	6.733e-01	4.451e-05	-4.845e-01
4	Ano/Cat	HCl	Asc	-7.706e-02	8.553e-02	1.277e-06	-5.022e-01
			Des	-9.978e-02	8.326e-02	1.765e-06	-5.090e-01
5	LPR	HCl	Asc	-1.185e-01	6.813e+09	5.268e-06	-5.033e-01
			Des	-1.345e+06	1.524e-01	6.876e-06	-5.086e-01
6	Ano/Cat	HCl	Asc	-7.490e-02	9.225e-02	1.469e-06	-4.806e-01
			Des	-1.035e-01	8.415e-02	2.140e-06	-5.097e-01
7	LPR	HCl	Asc	-8.758e-02	1.066e-01	1.995e-06	-4.879e-01
			Des	-1.422e-01	7.238e-02	2.008e-06	-4.938e-01

Scan	Type	Soln	Dir	$\sigma^2(A_{\text{H}})$	$\sigma^2(A_{\text{Fe}})$	$\sigma^2(j_{\text{corr}})$	$\sigma^2(\Delta\phi_{\text{corr}})$	n
0	Ano/Cat	H ₂ SO ₄	Asc	2.424e+02	2.786e+02	2.343e-15	1.401e-09	95
			Des	9.089e+00	1.206e+01	6.030e-15	3.785e-09	95
1	LPR	H ₂ SO ₄	Asc	2.201e-11	4.618e-11	3.857e-12	1.482e-08	346
			Des	2.857e-12	2.307e-12	4.525e-11	2.295e-08	346
2	Ano/Cat	H ₂ SO ₄	Asc	9.356e-06	1.890e-05	1.091e-13	3.618e-08	96
			Des	4.672e+00	8.336e+00	1.320e-14	7.072e-09	96
3	LPR	H ₂ SO ₄	Asc	5.563e-10	6.498e-10	7.818e-13	2.881e-08	349
			Des	1.988e-17	1.989e-17	1.538e-05	1.267e-08	349
4	Ano/Cat	HCl	Asc	3.771e+01	4.110e+01	1.809e-15	3.614e-09	97
			Des	1.705e+03	1.066e+03	1.665e-15	7.201e-10	97
5	LPR	HCl	Asc	4.081e-05	4.788e+16	1.440e-12	3.250e-08	360
			Des	4.067e+00	8.771e-04	2.186e-12	3.288e-08	360
6	Ano/Cat	HCl	Asc	4.333e+02	2.297e+02	1.349e-15	1.066e-09	97
			Des	3.935e+03	8.564e+03	1.584e-15	2.366e-10	97
7	LPR	HCl	Asc	1.088e-10	8.696e-11	3.508e-12	1.929e-08	342
			Des	1.436e-09	7.955e-10	1.933e-12	1.345e-08	342

Table 7: Derived parameters and variances for Equation 3 (Tafel slopes, corrosion currents, and corrosion potentials relative to SCE) for all 1018MS anodic/cathodic sweeps.

11 Appendix 3: Additional LPR Fits

Scan	Type	Soln	Dir	j_{corr} (A/mm ²)		
0	Ano/Cat	H ₂ SO ₄	Asc	1.230e-06		
			Des	1.247e-06		
1	LPR	H ₂ SO ₄	Asc	1.342e-06		
			Des	1.354e-06		
2	Ano/Cat	H ₂ SO ₄	Asc	1.219e-06		
			Des	2.870e-06		
3	LPR	H ₂ SO ₄	Asc	2.058e-06		
			Des	1.941e-06		
4	Ano/Cat	HCl	Asc	9.602e-07		
			Des	1.174e-06		
5	LPR	HCl	Asc	1.302e-06		
			Des	1.335e-06		
6	Ano/Cat	HCl	Asc	1.081e-06		
			Des	1.391e-06		
7	LPR	HCl	Asc	1.265e-06		
			Des	1.297e-06		
Scan	Type	Soln	Dir	$\Delta\phi_{\text{corr}}$ (V)	$\sigma^2(j_{\text{corr}})$	n
0	Ano/Cat	H ₂ SO ₄	Asc	-4.795e-01	4.861e-16	37
			Des	-4.835e-01	8.511e-15	38
1	LPR	H ₂ SO ₄	Asc	-4.830e-01	6.559e-16	338
			Des	-4.841e-01	3.434e-15	421
2	Ano/Cat	H ₂ SO ₄	Asc	-4.731e-01	7.537e-16	37
			Des	-4.839e-01	9.146e-14	39
3	LPR	H ₂ SO ₄	Asc	-4.822e-01	2.552e-15	342
			Des	-4.849e-01	1.070e-14	444
4	Ano/Cat	HCl	Asc	-5.030e-01	3.983e-15	38
			Des	-5.083e-01	2.566e-15	39
5	LPR	HCl	Asc	-5.032e-01	4.275e-14	353
			Des	-5.085e-01	2.300e-14	442
6	Ano/Cat	HCl	Asc	-4.814e-01	2.873e-15	38
			Des	-5.091e-01	2.515e-15	39
7	LPR	HCl	Asc	-4.879e-01	4.494e-15	342
			Des	-4.937e-01	2.720e-14	443

Table 8: Derived parameters and variances for Equation 3 (Tafel slopes, corrosion currents, and corrosion potentials relative to SCE) for all 1018MS anodic/cathodic sweeps.